Received: 29 May 2021 | Revised: 10 July 2021 | Accepted: 13 July 2021

DOI: 10.1002/fld.5033

RESEARCH ARTICLE

WILEY

An efficient and simplified Gay-Lussac approach in secondary variables form for the non-Boussinesq simulation of free convection problems

Peyman Mayeli | **Gregory J. Sheard**

Department of Mechanical and Aerospace Engineering, Monash University, Clayton, Victoria, Australia

Correspondence
Peyman Mayeli, Department of Mechanical and Aerospace Engineering, Monash University, Clayton, VIC 3800, Australia.
Email: peyman.mayeli@monash.edu

Funding information
National Computational Infrastructure; Australian Research Council, Grant/Award Number: DP180102647

Abstract

The Gay-Lussac (GL) approach is an incompressible-based strategy for non-Boussinesq treatment of the governing equations for free convection problems that is established based on extending the density variations beyond the gravity term. Such a strategy leads to emerging the GL parameter as a non-Boussinesq prefactor of different terms in the governing equations. In this article, the GL approach is expressed/discussed in terms of the secondary variables, that is, vorticity and stream-function, for the first time and a simplified version of this approach is proposed by removing density variations from the continuity equation. The difference of results under the simplified and traditional GL approach ranges within a maximum of 1% for different parameters. The lower computational cost of numerical solution of governing equations in the secondary variables formula and the corresponding convergence rate is scrutinized for the simplified GL approach showing around 25% lower computational cost. The performance of this approach is evaluated at high relative temperature differences against the low Mach number scheme and the Boussinesq approximations. In this respect, natural convection in an annulus cavity is numerically simulated using a CVFEM solver under the aforementioned approximations up to Rayleigh number $Ra = 10^5$ at Prandtl number $Pr = 1$ and high relative temperature differences ($\varepsilon = 0.15$ and 0.3). The largest deviations found for either the simplified GL or Boussinesq methods from the low Mach number scheme solution are less than 20% for velocity magnitude, 14% for stream function, 6% for vorticity, and 5% for temperature. Results under the three approximations are also analyzed in terms of the skin friction and local and average Nusselt number, indicating that the Gay-Lussac approach requires some revisions to act more accurately than the classical Boussinesq approximation at high relative temperature differences in natural convection problems, especially within the convection dominated regime.

KEYWORDS

annulus cavity, Gay-Lussac approximation, low Mach number scheme

1 | INTRODUCTION

Free convection related problems have myriad scientific and industrial applications, such as metallurgy processes, solar chimneys and collectors, astrophysical and geophysical phenomena, and so on.[1–5] Accurate prediction of the thermoflow fields within these systems when heat transfer mechanism is free convection dominated is of paramount importance. Traditionally, free convection problems are simulated numerically under the Boussinesq approximation that is also known as the Oberbeck–Boussinesq approximation. The Oberbeck–Boussinesq (OB) approximation is organized based on some basic assumptions: small temperature differences, negligible viscous heat dissipation in the energy equation, constant thermophysical properties of the working fluid, and small hydrostatic pressure variations across the height of the system. When these assumptions are satisfied, density variations negligibly affect the flow except the buoyancy term of the momentum equation. Using the volumetric thermal expansion coefficient, a linear state equation is derived as a function of temperature that makes the governing equations independent of explicit density variations.

The OB approximation is designed for natural convection phenomena associated by differential temperature difference featuring small order of compressibility but there are many situations, where the temperature nonuniformities generate significant density variations. In such situation, applying the classical OB approximation produces inaccurate results.[6] Literature survey indicates a few remedies that were proposed to overcome this issue. Different non-OB approximations for natural convention phenomena may be split into two major groups capturing compressible and incompressible approaches.

The first non-OB category is developed based on returning to the original essence of the natural convection phenomena by considering compressibility effects that invokes the Mach number. Generally speaking, actions toward compressible simulation of the Navier–Stokes equations is performed in two subcategories: fully compressible and weakly compressible approaches. However, the fully compressible approximation, in theory, is the optimal method for numerical simulation of free convection phenomena, but numerical complications caused by low-order compressibility ratio is a serious hindrance to its application. This approach was used by Darbandi and Hosseinizadeh,[7] Harish and Venkatasubbaiah,[8] and Busto et al..[9] The second remedy of the compressible non-OB category is the weakly compressible approach. In the weakly compressible approach that is often referred to as the low Mach number scheme (LMS), acoustic waves are filtered from the governing equation, which makes the method suitable for the compressible treatment of natural convection phenomena with small order of compressibility ratio. Under the LMS approximation, the total pressure is broken into two significant segments. The first segment is a spatially uniform pressure (known as the thermodynamic pressure) that comes from the equation of state by which the density is updated. The second segment is a local pressure (known as the hydrodynamic pressure) that acts just in the momentum equations. Armengol et al.[10] and Wan et al.[11] employed this algorithm for free convection phenomena with large temperature differences beyond the validity of the OB approximation.

The second category of the non-OB approximations rests on an incompressibility assumption. One of the non-OB strategies in this category is the Gay-Lussac (GL) approach that is established based on incorporating density variations beyond the gravity term of the momentum equations. This leads to the appearance of a dimensionless parameter, $Ga = \beta\Delta\theta$, where β is the isobaric expansion coefficient and $\Delta\theta$ a reference temperature. Following the OB approximation, a linear density state equation is employed to correlate density variations to the temperature differences. As will be shown later, Ga is equal to twice of the relative temperature difference. Under the GL approach, $(1 - Ga\Theta)$ emerges as a prefactor of different terms in the governing equations that acts as a modifier. Increasing Ga (e.g., invoking larger temperature differences) leads to an increase in deviation from the OB approximation. In Reference 12, the square cavity benchmark problem is studied by this strategy at large temperature differences. A GL-type approach is also possible by extending density variations just to one of the momentum or energy equations. For instance, Lopez et al.[13] proposed a GL-type approximation valid for rapidly rotating flows, whereby centrifugal contributions due to background rotation were captured via extension of density variations to the advection terms. Mayeli and Sheard[14,15] adopted a similar approach and showed that Ga may be cast in terms of Rayleigh, Prandtl, and Froude numbers, that is, $Ga = RaPrFr$.

Nonlinear density state relation,[16] temperature-dependent properties of the fluid[17] and also considering viscous friction and work of pressure stress terms of the energy equation (known as the thermodynamic Boussinesq model[18]) are other subcategories of the incompressible-based non-OB approximation strategies but for the sake of brevity, they are not discussed here. Different scenarios for the numerical simulation

of NC problems beyond the OB approximation in compressible and incompressible categories are reviewed in Reference 19.

The horizontal concentric annulus enclosure is a known benchmark problem in free convection related research. A comprehensive coverage was given in Kuhen and Goldstein.[20] Numerical contributions have also been made by References 20–28, where it is consistently reported that the two-dimensional solution remains time-invariant up to a Rayleigh number $Ra = 10^5$ at Prandtl numbers near unity. The interested reader is directed to the review by Reference 29.

In the present study, the annulus cavity problem is studied at high relative temperature differences under the three approximations including LMS, GL, and OB approximations. In this respect, governing equations under the GL approach are presented in secondary variable formulas (vorticity stream-function) for the first time. The following sections of the article are arranged as follows: Governing equations under the three approximations are presented in Section 2. The geometry, boundary conditions and numerical algorithms used in this work are introduced in Section 3. In Section 4, mismatches between the three approximations are interrogated via measurements of skin friction, local and average Nusselt number. A brief conclusion is given in Section 5.

2 | THE GAY-LUSSAC AND WEAKLY COMPRESSIBLE APPROACHES

Governing equations under the GL approach are extended beyond the OB approximation by taking into account density variations in any term of the governing equations in which density appears. Starting with the incompressible Navier–Stokes equations in the absence of any additional forces,

$$\begin{cases} (\rho/\rho_0)\nabla\cdot\boldsymbol{u} = 0, \\ \partial\boldsymbol{u}/\partial t^* + (\rho/\rho_0)(\boldsymbol{u}\cdot\nabla)\boldsymbol{u} = -(1/\rho_0)\nabla p + \nu\nabla^2\boldsymbol{u} + (\rho/\rho_0)\boldsymbol{e_g}, \\ \partial T/\partial t^* + (\rho/\rho_0)(\boldsymbol{u}\cdot\nabla)T = \alpha\nabla^2 T. \end{cases} \tag{1}$$

Following the OB approach, a linear density state relation ($\rho/\rho_0 = 1 - \beta\theta$) is substituted, and the following group of dimensionless parameters,

$$t = \frac{t^*\alpha}{L^2}, \boldsymbol{X} = \frac{\boldsymbol{x}}{L}, \boldsymbol{U} = \frac{\boldsymbol{u}L}{\alpha}, P = \frac{p^*L^2}{\rho\alpha^2}, \Theta = \frac{\theta}{\Delta\theta} = \frac{T - T_0}{T_h - T_c}, Ga = \beta\Delta\theta \tag{2}$$

the dimensionless form of the governing equation under the GL approximation are derived,

$$\begin{cases} (1 - Ga\Theta)\nabla\cdot\boldsymbol{U} = 0, \\ \partial\boldsymbol{U}/\partial t + (1 - Ga\Theta)(\boldsymbol{U}\cdot\nabla)\boldsymbol{U} = -\nabla P - RaPr\Theta\boldsymbol{e_g} + Pr\nabla^2\boldsymbol{U}, \\ \partial\Theta/\partial t + (1 - Ga\Theta)(\boldsymbol{U}\cdot\nabla)\Theta = \nabla^2\Theta. \end{cases} \tag{3}$$

As seen, as $Ga \to 0$ ($\Delta\theta \to 0$), the usual OB approximation is recovered. Under the GL approximation, $(1 - Ga\Theta)$ modifies different terms, and its effect becomes more pronounced by increasing Ga (and consequently $\Delta\theta$), but in practice Ga cannot exceed a specified value to avoid an unphysical (negative) density, that is,

$$\rho/\rho_0 = 1 - \beta\theta = 1 - \beta\Delta\theta\Theta = 1 - Ga\Theta > 0. \tag{4}$$

Equation (4) indicates the maximum Ga value in practice cannot exceed 2 ($Ga_{max} = 2$) based on defined dimensionless temperature. In Section 4, it is shown that by omitting density variations from the continuity equation, a simplified Gay-Lussac (SGL) approximation is obtained that yields identical results with the traditional GL approach,

$$\begin{cases} \nabla\cdot\boldsymbol{U} = 0, \\ \partial\boldsymbol{U}/\partial t + (1 - Ga\Theta)(\boldsymbol{U}\cdot\nabla)\boldsymbol{U} = -\nabla P - RaPr\Theta\boldsymbol{e_g} + Pr\nabla^2\boldsymbol{U}, \\ \partial\Theta/\partial t + (1 - Ga\Theta)(\boldsymbol{U}\cdot\nabla)\Theta = \nabla^2\Theta. \end{cases} \tag{5}$$

For comparison purposes, the problem is also simulated under the low Mach number scheme. The dimensionless low-Mach-number governing equations[19] are,

$$\begin{cases} \frac{\partial \rho}{\partial t} + \nabla \cdot (\rho \boldsymbol{U}) = 0, \\ \frac{\partial (\rho \boldsymbol{U})}{\partial t} + \nabla \cdot (\rho \boldsymbol{U} \otimes \boldsymbol{U}) = -\nabla P + \frac{RaPr}{2\varepsilon} \rho \boldsymbol{e}_g + Pr \nabla \cdot \boldsymbol{\tau}, \\ \frac{\partial (\rho \Theta)}{\partial t} + \nabla \cdot (\rho \boldsymbol{U} \Theta) = \nabla^2 \Theta + \left(\frac{\gamma - 1}{\gamma} \right) \frac{\mathrm{d}P_{\mathrm{th}}}{\mathrm{d}t}, \\ P_{\mathrm{th}} = \rho \Theta. \end{cases} \tag{6}$$

The following parameters have been used for dimensionless analysis of Equation (6),

$$\Theta = \frac{T}{T_0}, P_{\mathrm{th}} = \frac{p_{th}}{p_0}, \rho = \frac{\rho^*}{\rho_0}, t = \frac{t^* \alpha}{L^2}, \boldsymbol{X} = \frac{\boldsymbol{x}}{L_{ref}}, \boldsymbol{U} = \frac{\boldsymbol{u} L_{ref}}{\alpha}, P = \frac{p^* L_{ref}^2}{\rho \alpha^2}. \tag{7}$$

In Equation (6), P_{th} is the spatially uniform thermodynamic pressure, ε is the relative temperature difference ($\varepsilon = \Delta\theta / 2T_0$), and γ stands for heat capacity ratio ($\gamma = c_p / c_v$). When Stokes' hypothesis is applied for the bulk viscosity, the stress tensor is expressed as follows,

$$\boldsymbol{\tau} = \nabla \boldsymbol{U} + (\nabla \boldsymbol{U})^T - 2/3 (\nabla \cdot \boldsymbol{U}) \boldsymbol{I}. \tag{8}$$

The relative temperature difference that is applied for compressible simulation of natural convection problems may be related to the GL parameter by

$$\underbrace{2\varepsilon = (T_{\mathrm{h}} - T_{\mathrm{c}}) / T_o}_{\text{Compressible}} = \underbrace{\beta \Delta\theta = Ga}_{\text{Incompressible}}. \tag{9}$$

Using the vorticity ($\omega = \partial V / \partial X - \partial U / \partial Y$) and stream-function ($U = \partial \psi / \partial Y; V = -\partial \psi / \partial X$) parameters, the secondary variables form of the governing equations under the SGL approximation become

$$\begin{cases} \frac{\partial^2 \psi}{\partial X^2} + \frac{\partial^2 \psi}{\partial Y^2} = -\omega \\ \frac{\partial \omega}{\partial t} + (1 - 2\varepsilon\Theta) \left(\frac{\partial \psi}{\partial Y} \frac{\partial \omega}{\partial X} - \frac{\partial \psi}{\partial X} \frac{\partial \omega}{\partial Y} \right) = Pr \left(\frac{\partial^2 \omega}{\partial X^2} + \frac{\partial^2 \omega}{\partial Y^2} \right) + RaPr \frac{\partial \Theta}{\partial X}, \\ \frac{\partial \Theta}{\partial t} + (1 - 2\varepsilon\Theta) \left(\frac{\partial \psi}{\partial Y} \frac{\partial \Theta}{\partial X} - \frac{\partial \psi}{\partial X} \frac{\partial \Theta}{\partial Y} \right) = \frac{\partial^2 \Theta}{\partial X^2} + \frac{\partial^2 \Theta}{\partial Y^2}. \end{cases} \tag{10}$$

Similar to the primitive variables formulas, governing equations under the OB approximation are recovered as $\varepsilon \to 0$.

3 | THE ANNULUS ENCLOSURE AND NUMERICAL CONSIDERATIONS

The concentric horizontal annulus enclosure is studied at high relative temperature differences under the three approximations. Figure 1 shows the system under investigation. r_o and r_i are respectively the outer and inner enclosure radii. To be consistent with published benchmark studies,[20–24] the aspect ratio is fixed at $r_o - r_i / r_i = 1.6$. Applied boundary conditions in both primitive and secondary variables are shown in Figure 1(A). The gap between the two cylinders is filled with a working fluid with unity Prandtl number. The outer and inner cylinders are fixed at constant cold and hot temperatures, respectively. The gap between the two cylinders in the radial direction serves as the reference length, $L_{\mathrm{ref}} = r_o - r_i$. The two-dimensional steady flow is computed at Rayleigh numbers $10 \leq Ra \leq 10^5$ and relative temperature differences of 0.15 and 0.3. The computational domain is discretized with quadrilateral elements conforming to the circular domain, as shown in Figure 1(B). Elements are distributed uniformly in azimuth and are compressed toward the inner and outer cylinder surfaces to resolve the boundary layers.

Simulations are conducted using a solver employing a control volume finite-element method (CVFEM) for spatial discretization. In CVFEM, the physical domain is covered by a series of control volumes so that a unique finite volume is

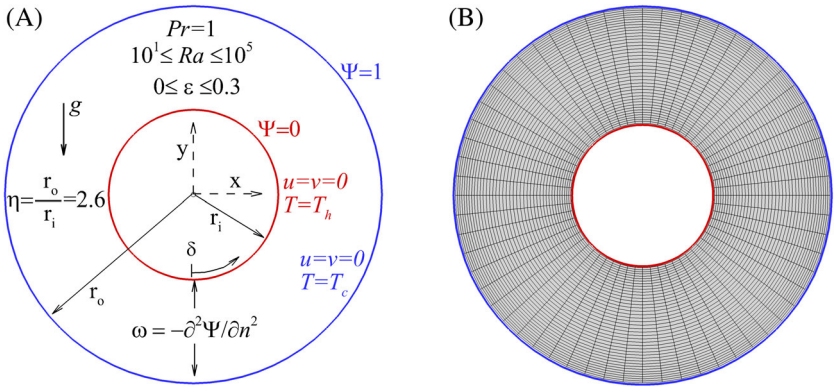

FIGURE 1 Concentric annulus enclosure. (A) Applied boundary conditions. (B) A coarse computational grid for illustration purposes [Colour figure can be viewed at wileyonlinelibrary.com]

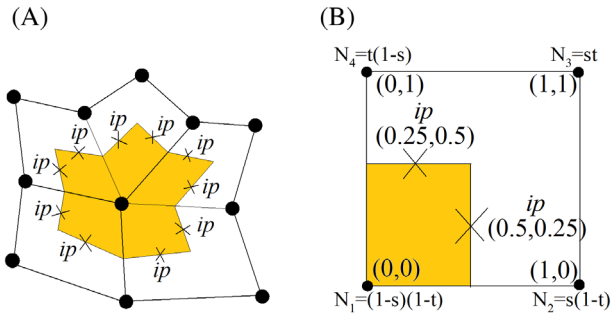

FIGURE 2 A schematic of quadrilateral elements. (A) A typical finite volume associated with integration points. (B) Local coordinate (s,t) and bilinear shape functions in a standard element [Colour figure can be viewed at wileyonlinelibrary.com]

allocated to each node as shown in Figure 2(A). Each control volume is encircled by several panels with an integration point (ip). Integration of Laplacian term over the finite volume yields

$$\int_{v_p} \nabla^2 \omega \mathrm{d}v = \oint_{A_p} \nabla \omega_{ip} \cdot \mathrm{d}\boldsymbol{A} = \sum_{ip=1}^{n} \nabla \omega_{ip} \cdot \boldsymbol{A_{ip}}. \tag{11}$$

In Equation (11), series counts for the number of ip encircling the main node where $\boldsymbol{A_{ip}}$ is corresponding to the normal vector of the surface at each ip. Under the CVFEM, bilinear shape functions ($N_j(s,t)$) are used to attribute the value of any parameter within the element to the nodal values via the weighted values,

$$\omega_{ip} = \omega(s,t) = \sum_{j=1}^{4} N_j(s,t)\omega_j. \tag{12}$$

The shape functions relating ip values to the nodal values in a quadrilateral element are shown in Figure 2(B). The Laplacian operator can be stated as follows

$$\mathrm{L}(\omega) = \sum_{ip=1}^{n}\sum_{j=1}^{4} \omega_j \nabla N_j \cdot \boldsymbol{A_{ip}}. \tag{13}$$

The effects of all nodes encircling an ip are involved in Equation (13) by weighted values that are identical to a central scheme. The Laplacian operator acts similarly in other equations.

The lagging technique is used to linearize the nonlinear terms in the governing equations. Integration of the advection term in secondary variables form over the finite volume and using data of the previous iteration for the lagged values

yields

$$\int_{v_p} (\bar{\psi}_y \omega_x - \bar{\psi}_x \omega_y) \mathrm{d}v = \oint A_p \bar{\psi}_y \omega \mathrm{d}A_x - \bar{\psi}_x \omega \mathrm{d}A_y = \oint A_p \omega (\bar{\psi}_y \mathrm{d}A_x - \bar{\psi}_x \mathrm{d}A_y) = \sum_{ip=1}^{n} \omega_{ip} (\bar{\psi}_{y_{ip}} A_{xip} - \bar{\psi}_{xip} A_{yip}). \tag{14}$$

Utilizing shape functions to approximate the integral point values to the nodal values yields

$$\mathrm{N}(\omega) = \sum_{ip=1}^{n} \sum_{j=1}^{4} \omega_j N_j (\bar{\psi}_{y_{ip}} A_{xip} - \bar{\psi}_{xip} A_{y_{ip}}). \tag{15}$$

Similarly, n in the series counts the number of ip encircling the main node in Equation (15). In linearization scheme, two storylines are possible to estimate the lagged values. In the first state, lagged values are approximated irrespective of the flow direction and weighted values determine the share of each node within the element, which leads to a central scheme. Another possible plan is estimating lagged values according to the flow direction at each ip that leads to the upwind scheme. It should be noted that velocity components are hidden in the vorticity and energy equations in terms of the stream-function, that is, $\bar{\psi}_{y_{ip}}$ and $-\bar{\psi}_{xip}$ for the horizontal and vertical components, respectively.

Solutions are advanced in time to a steady state using a second-order temporal scheme. A maximum difference of scalar values less than 10^{-7} during two successive steps is considered as the stop criteria for the iterative solution procedure. The solver has been validated in several previous studies.[30–34] A mesh resolution study was conducted on the present problem; it was determined that a mesh having 181 azimuthal and 91 radial elements provided six significant figures of accuracy for pertinent measured quantities.

In this study, natural convection in the considered geometry is studied in terms of the Nusselt number and skin friction. The local and average Nusselt numbers along the walls of the annulus enclosure are obtained from

$$Nu_{\mathrm{loc}} = -\partial \Theta / \partial \mathbf{n}|_{\mathrm{wall}} \tag{16}$$

and

$$Nu_{\mathrm{ave}} = \frac{1}{2\pi(r_i + r_o)} \left[\int_0^{2\pi r_o} Nu_{\mathrm{loc},o} \mathrm{d}s + \int_0^{2\pi r_i} Nu_{\mathrm{loc},i} \mathrm{d}s \right]. \tag{17}$$

The friction coefficient along the surface may be defined based on the dimensionless velocity

$$c_f = -\frac{\tau_w}{1/2\rho(\alpha/L)^2} = -2Pr \frac{\partial U_\delta}{\partial \boldsymbol{n}}\bigg|_{\mathrm{wall}}. \tag{18}$$

In the Cartesian coordinate system, the above fundamental definition for friction coefficient may be implemented through the following 2D shear stress tensor

$$\boldsymbol{c_f} = -2Pr \begin{bmatrix} \tau_{xx} & \tau_{xy} \\ \tau_{yx} & \tau_{yy} \end{bmatrix} \begin{bmatrix} n_x \\ n_y \end{bmatrix} = -2Pr \begin{bmatrix} 2\partial U/\partial X & \partial U/\partial Y + \partial V/\partial X \\ \partial U/\partial Y + \partial V/\partial X & 2\partial V/\partial Y \end{bmatrix} \begin{bmatrix} n_x \\ n_y \end{bmatrix}, \tag{19}$$

where n_x and n_y are the components of the wall-normal unit vector, respectively. The overall friction coefficient is then

$$c_f = \sqrt{(c_{fx})^2 + (c_{fy})^2}. \tag{20}$$

4 | ANALYZING RESULTS UNDER THE FULL AND SIMPLIFIED GAY-LUSSAC APPROACHES

In this section, it is demonstrated that the GL and SGL approaches give similar results in both transient and steady states. In other words, it is shown that the mismatch of the obtained results under the GL and SGL approaches is negligible with a reduced computational cost for the SGL approach. In this respect, the absolute difference in temperature, vorticity,

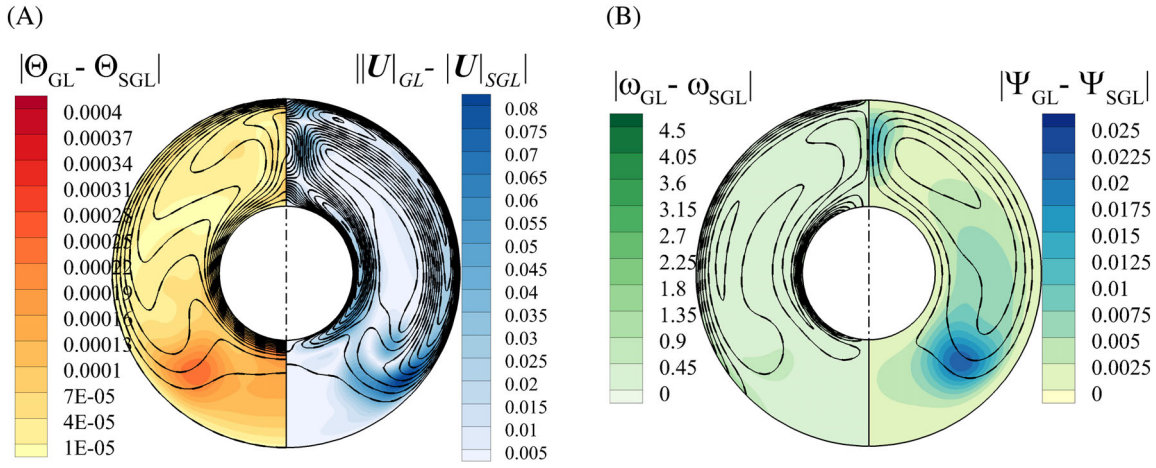

FIGURE 3 Comparing results under the GL and SGL approaches at $Ra = 10^5$, $Pr = 1$ and $Ga = 0.6$ for (A) absolute temperature and velocity magnitude difference and (B) absolute vorticity and stream-function difference. In both figures, solid and dashed lines show isovalues under the GL and SGL approximations, respectively [Colour figure can be viewed at wileyonlinelibrary.com]

stream-function and velocity magnitude at $Ra = 10^5$ and $Ga = 0.6$ ($\varepsilon = 0.3$), under the two approaches is calculated in steady state, and results are portrayed in Figure 3.

The maximum absolute temperature and velocity magnitude differences in Figure 3(A) are approximately 0.005 and 0.1, respectively, which ranges within 1% and 0.06% of the temperature and velocity magnitude values. Though the differences are very small, the largest differences in velocity magnitude are detected across the plume region and the middle height of the lower half of the enclosure adjacent to the outer cylinder. The first location corresponds to a strong free convection region where the working fluid leaves the inner hot cylinder toward a higher location close to the top cold boundary. The second location of large velocity magnitude differences corresponds to the region where the fluid becomes ready to start its vertical transport toward the highest location of the enclosure. The same difference pattern is observed for the stream-function in Figure 3(B) as expected while the vorticity difference has almost a uniform distribution over the physical domain in the same figure. The maximum absolute vorticity and stream-function differences in Figures 3(B) are approximately 5 and 0.03, respectively, which ranges within 0.14% and 0.12% of the vorticity and stream-function magnitude values.

Similar output/behavior of the GL and SGL approximations in the transient state is investigated in Figure 4 in the context of the absolute local Nusselt number and friction coefficient differences along the outer and inner cylinders at $Ra = 10^5$ and $Ga = 0.6$. Results indicate the absolute local Nusselt number difference is three orders smaller than the local Nusselt number magnitude during transient solution ($O(|\Delta Nu_{loc}|/Nu_{loc}) \sim 0.001$). A similar comparison for the absolute local friction coefficient difference shows a value of four order smaller value, that is, $O(|\Delta c_f|/c_f) \sim 10^{-4}$. Having demonstrated that the GL and SGL approximations exhibit identical behavior, we consider only the SGL approximation hereafter.

5 | ANALYZING COMPUTATIONAL COST AND CONVERGENCE HISTORIES OF THE PRIMARY AND SECONDARY VARIABLES FORMULAS

The secondary variables form of the governing equations are derived as an alternative to resolve the pressure coupling problem with the flow field. Nevertheless, the advantage of the secondary variables formula is not restricted to establish a coupling between the pressure and the velocity, but it has also a lower computational cost compared with the primary variables that are investigated in terms of the convergence rate and CPU time in this section.

To compare the computational cost of the iterative solution procedure, successive substeps at each iteration are explained for both primary and secondary variables formulas. For a consistent analysis, governing equations in both primary and secondary variables forms are advanced in time using a second-order Adams–Bashforth/Crank–Nicolson scheme in the context of a fractional step method having three substeps. For the primary variables, the first substep is

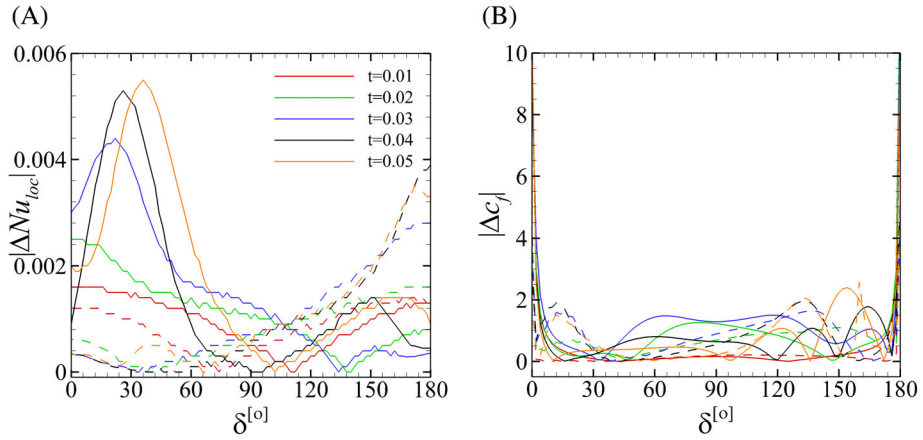

FIGURE 4 Comparing transient local Nusselt number and coefficient friction differences along the inner and outer cylinders under the GL and SGL approximations at $Ra = 10^5$, $Pr = 1$, and $Ga = 0.6$. (A) Absolute local Nusselt number differences and (B) absolute local coefficient friction differences. In both figures, solid lines represent data of the inner (hot) cylinder while dash lines represent data of the outer (cold) cylinder [Colour figure can be viewed at wileyonlinelibrary.com]

computing an intermediate velocity ($\boldsymbol{U}^*$) by solving the momentum equation in an explicit manner in the absence of the pressure term,

$$\frac{\boldsymbol{U}^* - \boldsymbol{U}^{\boldsymbol{n}}}{\Delta t} = -\frac{3}{2}(1 - 2\varepsilon\Theta^n)\mathrm{N}(\boldsymbol{U}^{\boldsymbol{n}}) + \frac{1}{2}(1 - 2\varepsilon\overline{\Theta^{n-1}})\mathrm{N}(\boldsymbol{U}^{\boldsymbol{n-1}}) + \frac{Pr}{2}\mathrm{L}(\boldsymbol{U}^{\boldsymbol{n}}) - RaPr\overline{\Theta^{n+1}}\boldsymbol{e_g}. \tag{21}$$

The second substep is applying the intermediate velocity accompanying by the pressure to the continuity equation, which yields a Poisson equation for the pressure, that is,

$$\nabla^2 P = \frac{1}{\Delta t}(\nabla \cdot \boldsymbol{U}^*). \tag{22}$$

The third substep is modifying the intermediate velocity using a pressure that satisfies a divergence-free condition for an incompressible flow field in an implicit manner,

$$\frac{\boldsymbol{U}^{\boldsymbol{n+1}} - \boldsymbol{U}^*}{\Delta t} = -\nabla P + \frac{Pr}{2}\mathrm{L}(\boldsymbol{U}^{\boldsymbol{n+1}}). \tag{23}$$

Equation (21) requires temperature information from the next time step in the buoyancy term. Thus, before updating the velocity field at each time step, the energy equation is advanced in time in the following two substeps,

$$\frac{\Theta^* - \Theta^n}{\Delta t} = -\frac{3}{2}(1 - 2\varepsilon\overline{\Theta^n})\mathrm{N}(\Theta^n) + \frac{1}{2}(1 - 2\varepsilon\overline{\Theta^{n-1}})\mathrm{N}(\Theta^{n-1}) + \frac{1}{2}\mathrm{L}(\Theta^n), \tag{24}$$

$$\frac{\Theta^{n+1} - \Theta^*}{\Delta t} = \frac{1}{2}\mathrm{L}(\Theta^{n+1}). \tag{25}$$

Similar to the primary variable, for the secondary variables formulas, the solution procedure at each time step starts with solving the energy equation in the two substeps explained by Equations (24) and (25). Then, the solution procedure continues with solving the vorticity and stream-function equations in the following substeps

$$\frac{\omega^* - \omega^n}{\Delta t} = -\frac{3}{2}(1 - 2\varepsilon\overline{\Theta^n})\mathrm{N}(\omega^n) + \frac{1}{2}(1 - 2\varepsilon\overline{\Theta^{n-1}})\mathrm{N}(\omega^{n-1}) + \frac{Pr}{2}\mathrm{L}(\omega^n) + RaPr\overline{\partial\Theta/\partial X^{n+1}}, \tag{26}$$

$$\frac{\omega^{n+1} - \omega^*}{\Delta t} = \frac{Pr}{2}\mathrm{L}(\omega^{n+1}), \tag{27}$$

$$\mathrm{D}(\psi^{n+1}) = -\overline{\omega^n}. \tag{28}$$

In general, solving Navier–Stokes and energy equations in the primary variable form with a second-order temporal accuracy requires solving seven equations for a 2D problem while the same problem may recast in five equations via the secondary variables.

Computational cost and convergence histories of the primary and secondary variables are compared in Figure 5. An inverse matrix of the Laplacian operator with appropriate boundary conditions is constructed for each of the equations that are being solved in an implicit manner to speed up the solution procedure. For instance, an inverted Laplacian matrix ($[D]^{-1}$) is multiplied by the vorticity vector at the right-hand side of Equation (28) to update the stream-function values in each iteration. CPU-time for a sample case having 121×81 elements is measured to compare the computational cost. Calculations were performed at $Ra = 10^5$ and $\epsilon = 0.3$ in two states in which the nonlinear operator acts based on upwind or central schemes. Bar charts of Figure 5(A) show an almost 25% lower computational cost for the secondary variables formulas compared with the primary one for both upwind and central schemes.

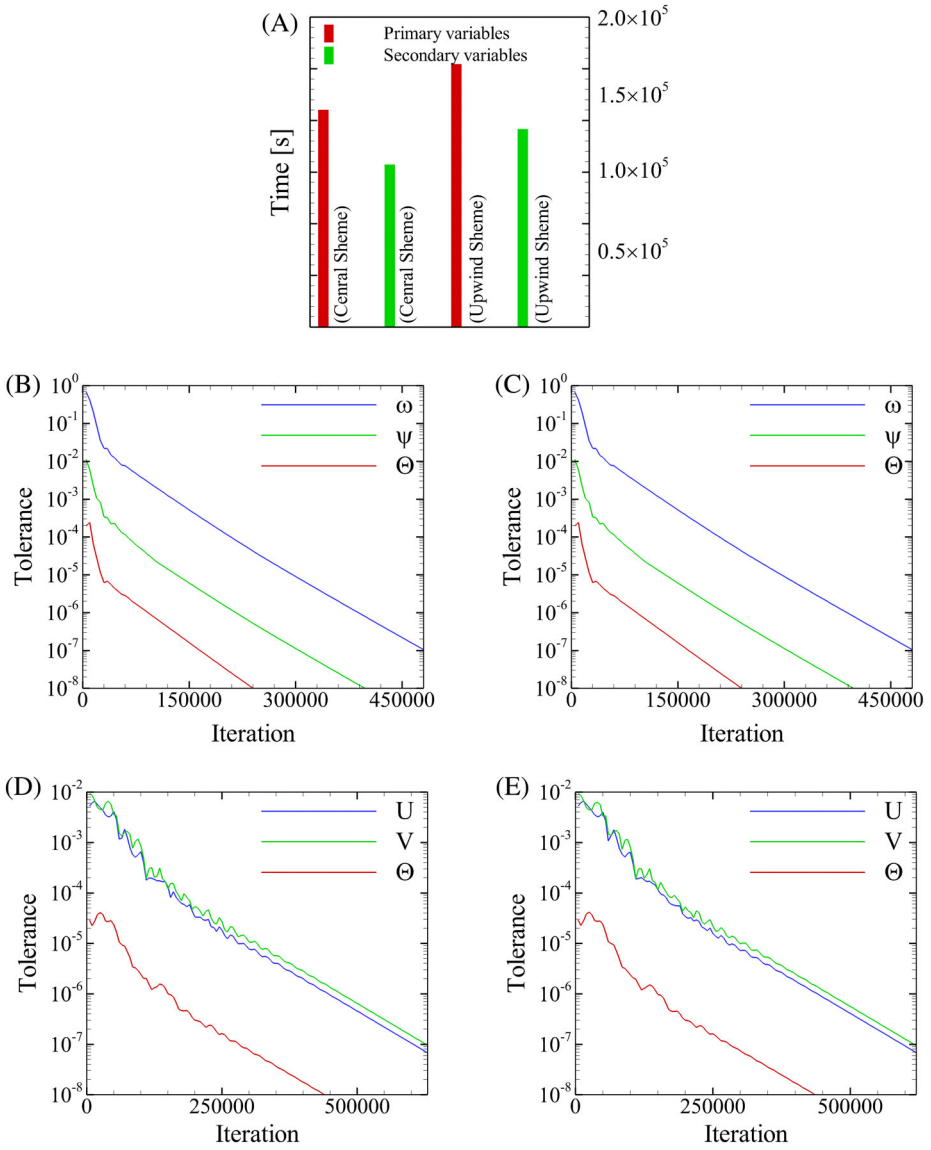

FIGURE 5 Computational cost and convergence histories of the computations at $Ra = 10^5$ and $\epsilon = 0.3$ using primitive and secondary variables. (A) CPU-time, (B) convergence rate of the secondary variables, central scheme; (C) convergence rate of the secondary variables, second-order upwind scheme; (D) convergence rate of secondary variables, second-order upwind; (E) convergence rate of the primitive variables, second-order upwind. A global time-step of 10^{-6} ($dt = 10^{-6}$) is used for calculations for all cases [Colour figure can be viewed at wileyonlinelibrary.com]

Convergence rates of the two approaches are also checked in terms of the variables tolerance during the iterative solution procedure through Figure 5(B–E). The tolerance of any parameter in this study is defined as the maximum alteration of all nodal values during two successive time-steps. Comparing convergence histories of the two approaches indicate that secondary variables form of the governing equations converges to a steady state with fewer oscillations. In addition, since both central and upwind schemes are applied in the second-order form, the differences in the convergence histories are not much different in each category.

6 | ANALYZING RESULTS UNDER THE LOW MACH NUMBER SCHEME, SIMPLIFIED GAY-LUSSAC, AND OBERBECK–BOUSSINESQ APPROXIMATIONS AT HIGH RELATIVE TEMPERATURE DIFFERENCES

Results under the three aforementioned approximations are analyzed in terms of the skin friction and local and average Nusselt number, in this section. For a deep analyze of the thermoflow fields, temperature, stream-function, velocity magnitude and vorticity fields under the LMS approximation are compared against the incompressible approaches in Figure 6(A–D), respectively, at $Ra = 10^5$ and $\varepsilon = 0.3$ ($Ga = 0.6$). It is apparent from the similar patterns traced by the solid and dashed contour lines, corresponding respectively to the weakly compressible and incompressible approaches, that both approaches correctly capture the essential thermal and kinematic features of the system. The largest deviations found for either the GL or OB methods from the LMS solution are less than 20% for velocity magnitude, 14% for stream function, 6% for vorticity and 5% for temperature. Local measurements are notoriously sensitive to small changes in the location and strength of structures within a flow; in support of the efficacy of the tested approaches, it will be shown later that integrated quantities obtained from these solutions, including Nusselt number, exhibit even smaller differences. Figure 6(D) demonstrates that the vorticity field is captured exceptionally well using both the GL and OB methods. The largest deviations are experienced in both cases within a layer of fluid just outside the boundary layer on either side of the inner cylinder. The contour lines in Figure 6(C) reveal that this layer corresponds to fast-moving fluid entrained in buoyant jets ascending around each side of the cylinder. Both the GL and OB methods produce deviations in velocity magnitude that are greatest on the outer side of these fast-moving jets. These deviations extend upward from the top of the inner cylinder, straddling the buoyant plume that rises on the vertical centerline of the cavity. The GL approach exhibits slightly stronger velocity magnitude deviations than the OB approach in the jet, while the OB approach deviates more toward the sides of the outer cylinder, in the part of the flow that descends adjacent to the cooler outer cylinder.

The most visible differences between the GL and OB methods may be found in the stream-function fields plotted in Figure 6(B). The stream-function is zero along the vertical plane of symmetry and on both cylinder surfaces, and rises in the interior of the fluid on both sides of the cavity. This reflects the circulating flow generated by the natural convective transport of heat from the inner cylinder, up to the top of the cavity, before cooling and descending adjacent to the outer cylinder toward the bottom of the cavity. Both the GL and OB approaches show the largest deviations in stream-function in the upper quadrants of the cavity, close to the core of the circulations. The GL approach exhibits deviations extending down to the side of the cylinder, outside the fast-moving jet around the inner cylinder, while the OB method is relatively weaker in that region, instead manifesting a stronger zone in the lower quadrant of the cavity.

Finally, the temperature deviations are qualitatively similar between the GL and OB approaches. The GL approach exhibits slightly larger differences within the large overturning natural convection cell. By contrast, stronger deviations are seen under the OB approach at the top of the plume near the upper surface of the outer cylinder. It becomes apparent that under high-temperature differences, neither the OB nor the GL method is universally superior; care must be taken to determine which quantity(s) of interest may be better captured by which method. The distributions of the local Nusselt number and skin friction coefficients presented in the sections to follow provide further insights as to which approach may be more suitable, depending on the governing parameter values and local features of a flow.

The magnitude of the non-OB terms in the momentum and energy equations in secondary variable formulas are portrayed in Figure 7. These are indeed the terms that are appeared by taking into account density variations beyond the gravity term. The magnitude of the non-OB term in the momentum equation, that is, $|\Theta(\partial\psi/\partial Y\partial\omega/\partial X - \partial\psi/\partial X\partial\omega/\partial Y)|$ in Figure 7(A), is larger across the upper half of the inner cylinder and end of the plume region colliding the highest height of the cavity. These are the regions that isovorticity lines are accumulated in Figure 6(D) leading to larger vorticity gradients. A similar distribution of the non-OB term in the energy equation, that is, $|\Theta(\partial\psi/\partial Y\partial\Theta/\partial X - \partial\psi/\partial X\partial\Theta/\partial Y)|$ is

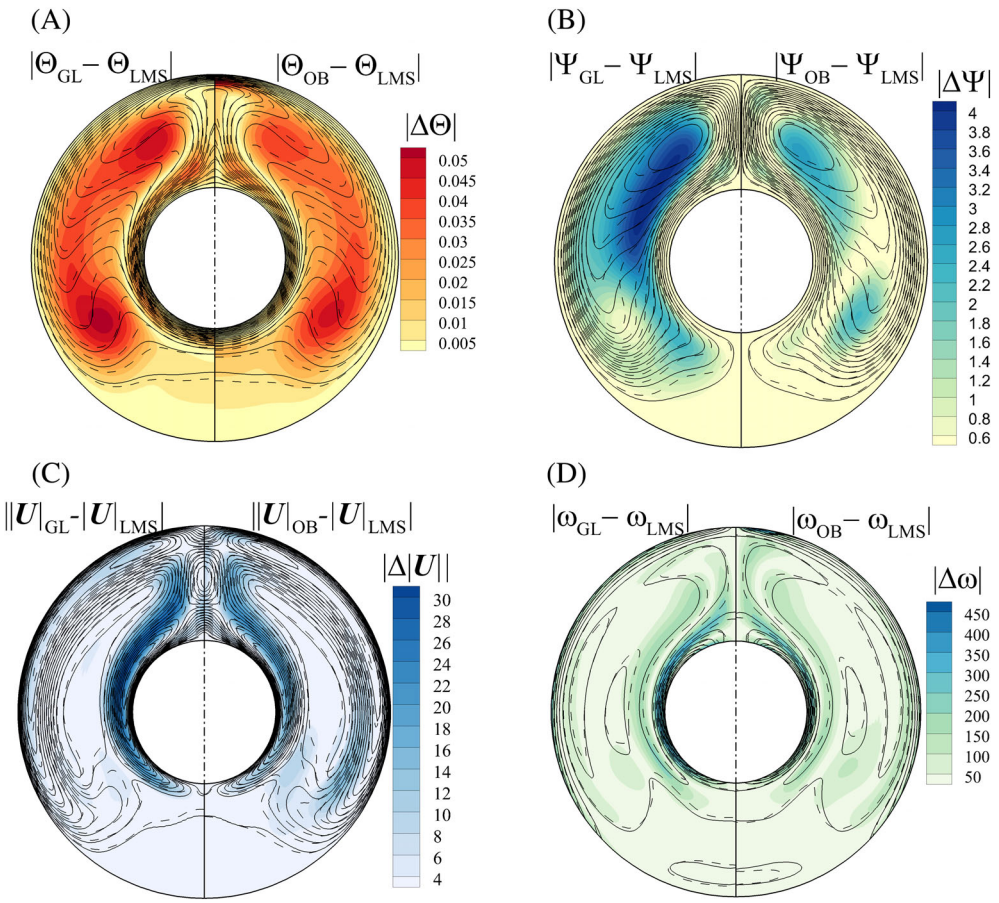

FIGURE 6 Absolute differences of results under the LMS, GL, and OB approximations at $Ra = 10^5$ and $\varepsilon = 0.3$ for (A) temperature, (B) stream-function, (C) velocity magnitude, and (D) vorticity. In all figures, the left half shows the difference between the LMS and GL approximations while the right half depicts the difference between the LMS and OB approximations. Solid lines in all figures represent the isovalues of the parameter under the LMS approximation while dash lines show the incompressible approach [Colour figure can be viewed at wileyonlinelibrary.com]

observable in Figure 7(B). Regions having larger temperature gradients amplify the non-OB term in the energy equation. Accumulation of the isotherm-lines in Figure 6(A) is in agreement with the regions having stronger non-OB term in the energy equation, however, a comparison of the result against the LMS approximation reveals that the non-OB terms are not efficiently modifying thermoflow field at larger temperature differences.

6.1 | Local Nusselt number

The local Nusselt number under the three approximations is investigated at the highest Rayleigh number ($Ra = 10^5$) and respective relative temperature differences $\varepsilon = 0.15$ and 0.3 in Figure 8(A,B), respectively. As seen, the two incompressible approaches show similar behavior, both deviating from the LMS approximation. Along the outer cylinder, the SGL approach shows more accurate results compared with the OB approximation at about $\delta \approx 170$ with $\varepsilon = 0.3$ (Figure 8(B)) compared with $\varepsilon = 0.15$ (Figure 8(A)). For the inner cylinder, there is a visible gap among the local Nusselt number values at smaller δ under the incompressible and LMS approximations that becomes more visible by increasing ε. Also by increasing ε, the SGL approach shows more deviation from the LMS approximation at about $0 \lesssim \delta \lesssim 25^{\circ}$ compared with the OB approximation.

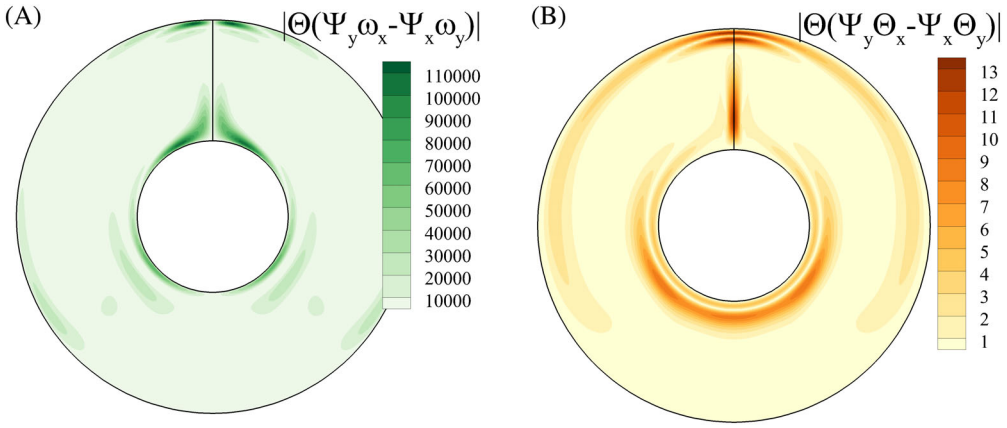

FIGURE 7 The magnitude of the non-OB terms at $Ra = 10^5$ in secondary variable form of the governing equations in (A) vorticity equation and (B) energy equation [Colour figure can be viewed at wileyonlinelibrary.com]

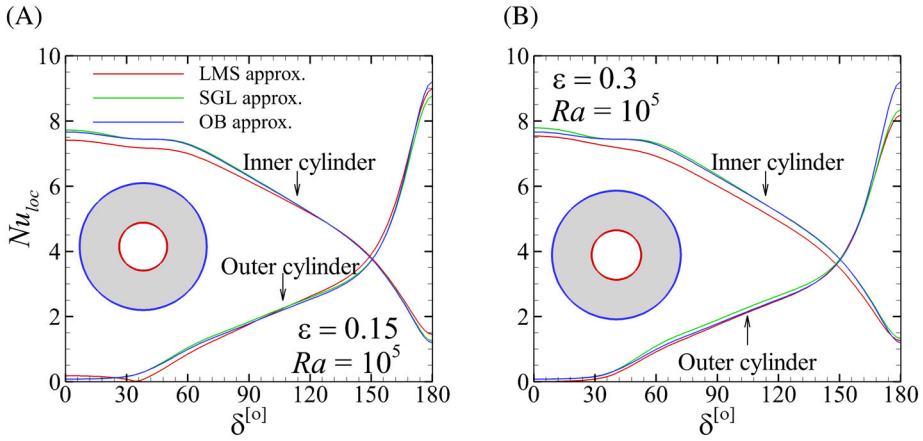

FIGURE 8 Comparing the local Nusselt number under the LMS and incompressible approximations along the inner and outer surfaces at $Ra = 10^5$ and (A) $\varepsilon = 0.15$, (B) $\varepsilon = 0.3$ [Colour figure can be viewed at wileyonlinelibrary.com]

6.2 | Average Nusselt number

The average Nusselt number was calculated from the simulations spanning $10^1 \leq Ra \leq 10^5$, and is plotted in Figure 9(A,B) for $\varepsilon = 0.15$ and 0.3, respectively. Equation (12) is evaluated by Simpson's one-third rule. Below $Ra \approx 10^2$, Nusselt number was found to be approximately constant at both relative temperature values. In this regime, thermal conduction dominates. As Rayleigh number increases to $Ra \approx 10^3$, the flow evolves into a state dominated by thermal convection, beyond which Nusselt number follows approximately to a power-law going as $Nu \sim Ra^4$.

In the low-Ra regime, the average Nusselt number is indistinguishable between the three methods. This follows from the conduction-dominated nature of this regime, where advection, convection, and buoyancy contribute negligibly to the flow, this suppressing the very components of the respective sets of governing equations that differ between the three methods. In the higher-Ra regime, the results obtained for $\varepsilon = 0.15$ are differed by a smaller amount between the three methods when compared with the results at $\varepsilon = 0.3$. Interestingly, at both $\varepsilon = 0.15$ and 0.3, the OB and SGL approximations yield almost the same results, with both slightly over-estimating the Nusselt number when compared with the LMS method. At $Ra = 10^5$ and $\varepsilon = 0.3$, respective mismatches in average Nusselt numbers of 4.8% and 4.2% for the SGL and OB approximations are found when compared with the LMS method.

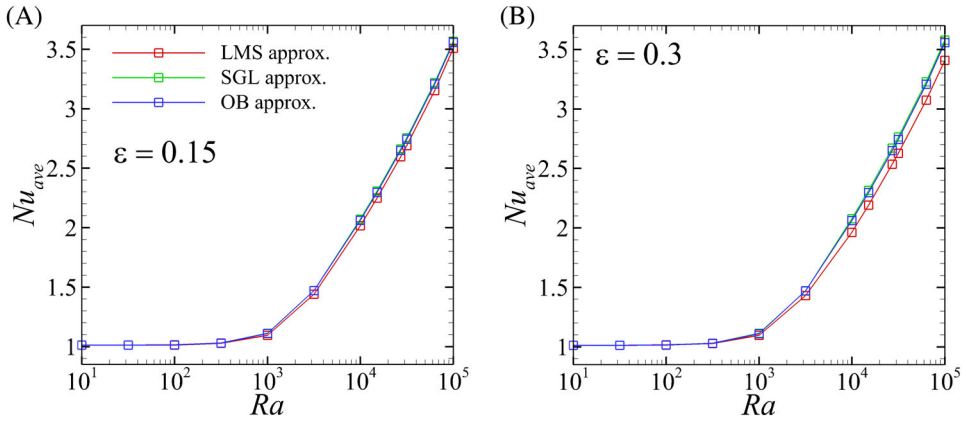

FIGURE 9 Comparing the average Nusselt number under the low Mac number scheme and two incompressible approximations at $10^1 \leq Ra \leq 10^5$ and (A) $\varepsilon = 0.15$, (B) $\varepsilon = 0.3$ [Colour figure can be viewed at wileyonlinelibrary.com]

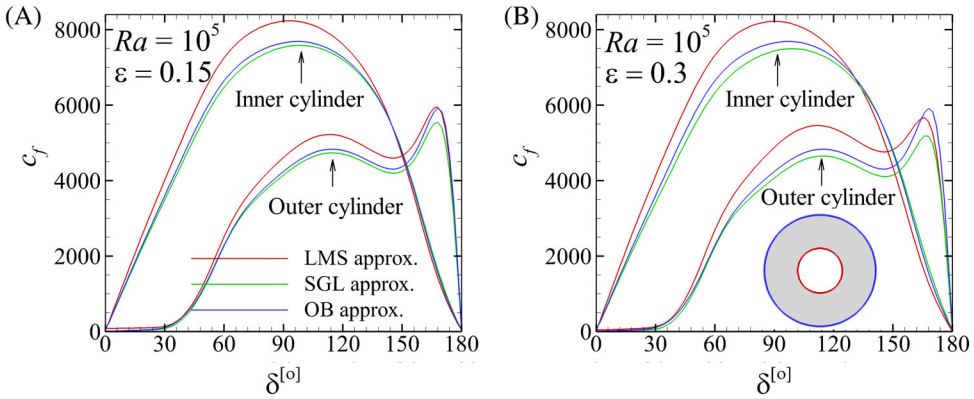

FIGURE 10 Comparing the local coefficient friction results under the two incompressible and LMS approximations along the inner and outer surfaces at $Ra = 10^5$ and (A) $\varepsilon = 0.15$, (B) $\varepsilon = 0.3$ [Colour figure can be viewed at wileyonlinelibrary.com]

6.3 | Skin shear stress

The coefficient of friction is the final considered parameter in this study. Results are plotted for the inner and outer cylinders at $Ra = 10^5$ and $\varepsilon = 0.15$ and 0.3 in Figure 10(A,B), respectively. Both incompressible approaches show a visible mismatch against the LMS approximation. For the inner (hot) cylinder, the mismatch is larger at $50 \lesssim \delta \lesssim 170$ but for the outer (cold) cylinder the mismatch is detected at $10 \lesssim \delta \lesssim 110$. The results indicate that increasing the relative temperature difference from 0.15 to 0.3 leads to the SGL approach deviating from the LMS approximation compared with the OB approximation. This deviation (also detected in the Nusselt number data) may be ascribed to the inappropriate density state equation that is used to extend density variations beyond the gravity term under the SGL approximation.

7 | CONCLUSION

Free convection in a concentric annulus enclosure is studied numerically at high relative temperature differences ($\varepsilon = 0.15$ and 0.3) up to Rayleigh number $Ra = 10^5$ and a fixed Prandtl number of unity under the low Mach number and an incompressible non-Boussinesq approximation known as the Gay-Lussac approach. The non-Boussinesq approximation is established based on extending density variations beyond the gravity term of the momentum equations. In this respect, governing equations under the Gay-Lussac approach are presented in vorticity stream-function form. The problem is also simulated under the classical Oberbeck–Boussinesq approximation and results are evaluated in terms of the absolute differences in temperature, stream-function, velocity magnitude, and vorticity fields. These comparisons

show a considerable mismatch among the compressible and incompressible approximations at high relative temperature differences, even for the applied non-Boussinesq approach. In other words, obtained results under the Gay-Lussac approach do not show a clear superiority compared with the Oberbeck–Boussinesq approximation. Results of the incompressible approaches are also compared against the weekly compressible approach in terms of the skin friction and local and average Nusselt number, confirming that the Gay-Lussac approach requires further treatments/revisions to surpass the performance of the Boussinesq approximation. Finally, a computational cost analysis confirms that solving governing equations in the presented secondary variable formulas reduces the computational cost by around 25% compared with the primary variables formulas.

ACKNOWLEDGMENTS

This research was supported by the Australian Research Council through Discovery Project DP180102647. Peyman Mayeli is supported by a Monash Graduate Scholarship and a Monash International Postgraduate Research Scholarship. The authors are also supported by time allocations on the National Computational Infrastructure (NCI) peak facility and the Pawsey Supercomputing Centre through NCMAS grants. NCI is supported by the Australian Government.

CONFLICT OF INTEREST

The authors declare no conflict of interest.

DATA AVAILABILITY STATEMENT

Data sharing is not applicable as no new data generated.

NOMENCLATURE

c_f	skin friction coefficient
Ga	Gay-Lussac parameter ($\beta\Delta\theta$)
L	Laplacian operator
L_{ref}	reference length
$\boldsymbol{n}$	unit normal vector to the surface
N	nonlinear operator
Nu_{ave}	average Nusselt number
Nu_{loc}	local Nusselt number
p^*	modified pressure
P	dimensionless pressure
P_{th}	thermodynamic pressure
Pr	Prandtl number
r	radius
Ra	Rayleigh number
T	temperature
$\boldsymbol{u}$	velocity vector
$\boldsymbol{U}$	dimensionless velocity vector
$\boldsymbol{x}$	coordinate vector
$\boldsymbol{X}$	dimensionless coordinate vector
α	thermal diffusivity
β	isobaric expansion coefficient
γ	heat capacity ratio
ε	relative temperature difference
θ	physical temperature
Θ	dimensionless temperature
ρ	density
ν	kinematic viscosity
τ_w	wall shear stress
ψ	stream-function
ω	vorticity

SUBSCRIPT

ave	average
loc	local
0	reference value

SUPERSCRIPT

n	current time-step
$n-1$	previous time-step
—	refers to a lagged value

ORCID

Peyman Mayeli https://orcid.org/0000-0003-4084-2627

REFERENCES

1. Buchberg H, Catton I, Edwards DK. Natural convection in enclosed spaces—a review of application to solar energy collection. *ASME J Heat Transf*. 1976;98(2):182-188.
2. Tonui JK, Tripanagnostopoulos Y. Performance improvement of PV/T solar collectors with natural air flow operation. *Sol Energy*. 2008;82(1):1-12.
3. Phiraphat S, Prommas R, Puangsombut W. Experimental study of natural convection in PV roof solar collector. *Int Commun Heat Mass Transf*. 2017;89:31-38.
4. Van Dam RL, Simmons CT, Hyndman DW, Wood WW. Natural free convection in porous media: first field documentation in groundwater. *Geophys Res Lett*. 2008;609:111-137. https://doi.org/10.1029/2008GL036906
5. Sparrow EM, Patankar SV, Ramadhyani S. Analysis of melting in the presence of natural convection in the melt region. *ASME J Heat Transf*. 1977;99(4):520-526.
6. Paillere H, Viozat C, Kumbaro A, Toumi I. Comparison of low Mach number models for natural convection problems. *Heat Mass Transf*. 2000;36:567-573.
7. Darbandi M, Hosseinizadeh SF. Numerical study of natural convection in vertical enclosures using a novel non-Boussinesq algorithm. *Numer Heat Transf A*. 2007;52:849-873.
8. Harish R, Venkatasubbaiah K. Numerical investigation of instability patterns and nonlinear buoyant exchange flow between enclosures by variable density approach. *Comput Fluids*. 2014;96:276-287.
9. Busto S, Tavelli M, Boscheri W, Dumbser M. Efficient high order accurate staggered semi-implicit discontinuous Galerkin methods for natural convection problems. *Comput Fluids*. 2020;198:104399.
10. Armengol JM, Bannwart FC, Xaman J, Santos RG. Effects of variable air properties on transient natural convection for large temperature differences. *Int J Therm Sci*. 2017;120:63-79.
11. Wan ZH, Wang Q, Wang B, Xia SN, Zhou Q. On non-Oberbeck–Boussinesq effects in Rayleigh–Bénard convection of air for large temperature differences. *J Fluid Mech*. 2020;889:A10.
12. Pesso T, Piva S. Laminar natural convection in a square cavity: low prandtl numbers and large density differences. *Int J Heat Mass Transf*. 2009;52(3–4):1036-1043.
13. Lopez JM, Marques F, Avila M. The Boussinesq approximation in rapidly rotating flows. *J Fluid Mech*. 2013;737(2013):56-77.
14. Mayeli P, Sheard G. A new formulation for Boussinesq-type natural convection flows applied to the annulus cavity problem. *Int J Numer Methods Fluids*. 2021;93(3):683-702.
15. Mayeli P, Sheard G. Natural convection and entropy generation in square and skew cavities due to large temperature differences: a gay-Lussac type vorticity stream-function approach. *Int J Numer Methods Fluids*. 2021;93(7):2396-2420.
16. Lee CH, Hyun JM, Kwak HS. Oscillatory enclosed buoyant convection of a fluid with the density maximum. *Int J Heat Mass Transf*. 2000;43(19):3747-3751.
17. Zhong ZY, Yang KT, Lioyd JR. Variable property effects in laminar natural convection in a square enclosure. *ASME J Heat Transf*. 1985;107:133-138.
18. Pons M, Le Quéré P. Modeling natural convection with the work of pressure-forces: a thermodynamic necessity. *Int J Numer Methods Heat Fluid Flow*. 2007;17(3):322-332.
19. Mayeli P, Sheard GJ. Buoyancy-driven flows beyond the Boussinesq approximation: a brief review. *Int Commun Heat Mass Transf*. 2021;125:105316.
20. Kuhen TH, Goldstein RJ. An experimental and theoretical study of natural convection in the annulus between horizontal concentric cylinders. *J Fluid Mech*. 1976;74(4):695-719.
21. Abu-Nada E, Masoud Z, Hijazi A. Natural convection heat transfer enhancement in horizontal concentric annuli using nanofluids. *Int Commun Heat Mass Transf*. 2008;35:657-665.
22. Ashrafizadeh A, Nikfar M. On the numerical solution of generalized convection heat transfer problems via the method of proper closure equations–part II: application to test problems. *Numer Heat Transf B*. 2016;70(2):204-222.
23. Ashorynejad HR, Mohamad AA, Sheikholeslami M. Magnetic field effects on natural convection flow of a nanofluid in a horizontal cylindrical annulus using lattice Boltzmann method. *Int J Therm Sci*. 2013;64:240-250.

24. Wu YL, Liu GR, Gu YT. Application of Meshless local Petrov-Galerkin (MLPG) approach to simulation of incompressible flow. *Numer Heat Transf B*. 2005;48(5):459-475.
25. Shadlaghani A, Farzaneh M, Shahabadi M, Tavakoli MR, Safaei MR, Mazinani I. Numerical investigation of serrated fins on natural convection from concentric and eccentric annuli with different cross sections. *J Therm Anal Calorim*. 2019;135:1429-1442.
26. Afrand M, Sina N, Teimouri H, et al. Effect of magnetic field on free convection in inclined cylindrical annulus containing molten potassium. *Int J Appl Mech*. 2015;7(4):1550052.
27. Rozati SA, Montazerifar F, Ali Akbari O, et al. Natural convection heat transfer of water/Ag nanofluid inside an elliptical enclosure with different attack angles. *Math Methods Appl Sci*. https://doi.org/10.1002/mma.7036
28. Malvandia A, Safaei MR, Kaffash MH, Ganji DD. MHD mixed convection in a vertical annulus filled with Al_2O_3–water nanofluid considering nanoparticle migration. *J Magn Magn Mater*. 2015;382:296-306.
29. Dawood HK, Mohammed HA, Sidikb NAC, Munisamy KM, Wahid MA. Forced, natural and mixed-convection heat transfer and fluid flow in annulus: a review. *Int Commun Heat Mass Transf*. 2015;62:45-47.
30. Mayeli P, Hesami H, Besharati-Foumani H, Niajalili M. Al2O3-water nanofluid heat transfer and entropy generation in a ribbed channel with wavy wall in the presence of magnetic field. *Numer Heat Transf A*. 2018;73(9):604-623.
31. Hesami H, Mayeli P. Development of the ball-spine algorithm for the shape optimization of ducts containing nanofluid. *Numer Heat Transf A*. 2016;70(12):1371-1389.
32. Mayeli P, Nikfar M. Temperature identification of a heat source in conjugate heat transfer problems via an inverse analysis. *Int J Numer Methods Heat Fluid Flow*. 2019;29(10):3994-4010.
33. Mayeli P, Nili-Ahmadabadi M, Pirzadeh MR, Rahmani P. Determination of desired geometry by a novel extension of ball spine algorithm inverse method to conjugate heat transfer problems. *Comput Fluids*. 2017;154:390-406.
34. Mayeli P, Nili-Ahmadabadi M, Besharati-Foumani H. Inverse shape design for heat conduction problems via the ball spine algorithm. *Numer Heat Transf B*. 2016;69(3):249-269.

How to cite this article: Mayeli P, Sheard GJ. An efficient and simplified Gay-Lussac approach in secondary variables form for the non-Boussinesq simulation of free convection problems. *Int J Numer Meth Fluids*. 2021;93:3264-3279. doi: 10.1002/fld.5033